THE JOURNAL OF PHYSICAL CHEMISTRY LETTERS
A JOURNAL OF THE AMERICAN CHEMICAL SOCIETY

pubs.acs.org/JPCL

Letter

Accelerated Hot-Carrier Cooling in $MAPbI_3$ Perovskite by Pressure-Induced Lattice Compression

Loreta A. Muscarella, Eline M. Hutter, Jarvist M. Frost, Gianluca G. Grimaldi, Jan Versluis, Huib J. Bakker, and Bruno Ehrler*

Cite This: *J. Phys. Chem. Lett.* 2021, 12, 4118–4124

Read Online

ACCESS | Metrics & More | Article Recommendations | Supporting Information

ABSTRACT: Hot-carrier cooling (HCC) in metal halide perovskites above the Mott transition is significantly slower than in conventional semiconductors. This effect is commonly attributed to a hot-phonon bottleneck, but the influence of the lattice properties on the HCC behavior is poorly understood. Using pressure-dependent transient absorption spectroscopy, we find that at an excitation density below the Mott transition, pressure does not affect the HCC. On the contrary, above the Mott transition, HCC in methylammonium lead iodide is around 2−3 times faster at 0.3 GPa than at ambient pressure. Our electron−phonon coupling calculations reveal ∼2-fold stronger electron−phonon coupling for the inorganic cage mode at 0.3 GPa. However, our experiments reveal that pressure promotes faster HCC only above the Mott transition. Altogether, these findings suggest a change in the nature of excited carriers above the Mott transition threshold, providing insights into the electronic behavior of devices operating at such high charge-carrier densities.

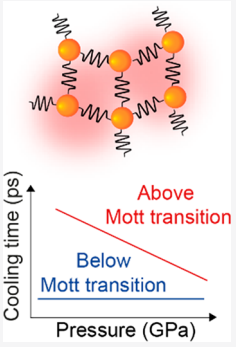

Photoexcitation with a photon energy larger than the bandgap of semiconductors results in the formation of a nonthermal distribution of "hot charge carriers" (i.e., high-energy electrons in the conduction band and high-energy holes in the valence band). In semiconductor solar cells, these charges relax to the conduction (and valence) band edge before they are collected. The first step is thermalization,[1,2] occurring within a few hundred femtoseconds, where the generated hot carriers interact with each other through carrier−carrier scattering until they reach a common quasi-Fermi temperature, usually much higher than the lattice temperature. Subsequently, hot-carrier cooling (HCC) occurs though carrier−phonon or carrier−impurity scattering until a thermal equilibrium with the local lattice is reached, usually on picosecond time scales.[1,3,4] In this step, heat is dissipated in the lattice through acoustic phonons. In solar cells, 33% of the energy of sunlight is lost as heat[5,6] during the thermalization and cooling processes. Slow HCC is desired for thermoelectric devices[7] and hot-carrier solar cells[8] where extracting carriers before they have cooled could enable breaking the thermodynamic limit for single-junction solar cells. Emissive applications such as lasers,[9] single-photon sources,[10] and optical modulators[11] require short HCC times for efficient radiative recombination and to prevent carrier trapping. In particular for lasers, understanding the electronic properties at high carrier density required to obtain lasing is essential.

In metal halide perovskites, the HCC time scale was found to be significantly slower[3,12−14] than in conventional semiconductors like InN[15] or GaAs[12] under the same (high) excitation density conditions. In addition, the HCCis slower with an increase in the excitation density.[3,16,17] This slower cooling has been explained from an effect that is commonly known as a hot-phonon bottleneck. The origin of this phenomenon is still under debate, but it has been attributed to several mechanisms such as the accumulation of optical phonons that cannot be easily dissipated,[12,18,3] optical−acoustic phonon upconversion,[14] and polaron formation.[19−21]

Metal halide perovskites are polar semiconductors, and thus, their electronic properties are expected to be strongly coupled with the lattice vibrations. Applying external pressure directly affects the lattice dynamics and therefore can be used to tune properties that are strongly dependent on the lattice vibrations, such as the electron−phonon coupling and the phonon lifetimes. Changes in one or both of these quantities can affect the HCC. Increasing the electron−phonon coupling is expected to lead to faster HCC. Replacing iodide with a lighter halide increases the frequency of the longitudinal optical phonon mode (ω_{LO})[22] and thus shortens the HCC time measured under the same excess of energy and excitation density conditions.[23,24,3] In $MAPbI_3$, the acoustic phonon lifetime, responsible for heat transport, has been found to be in the range of a few picoseconds,[25,26] 2 orders of magnitude shorter than in conventional semiconductors.[27] Thus, the thermal transport at room temperature in $MAPbI_3$ is highly

Received: March 2, 2021
Accepted: March 29, 2021

https://doi.org/10.1021/acs.jpclett.1c00676
J. Phys. Chem. Lett. 2021, 12, 4118–4124

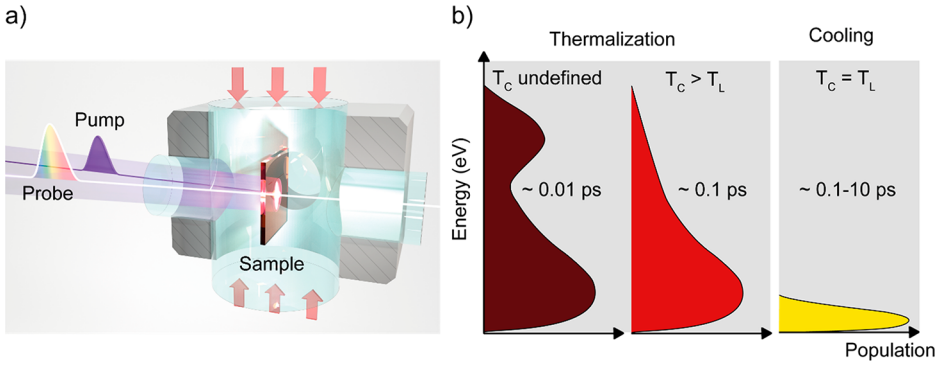

Figure 1. Schematic representation of the (a) pressure-dependent fs-TA setup showing the generation of hot carriers (white spot on the sample) and (b) HCC mechanism following photoexcitation.

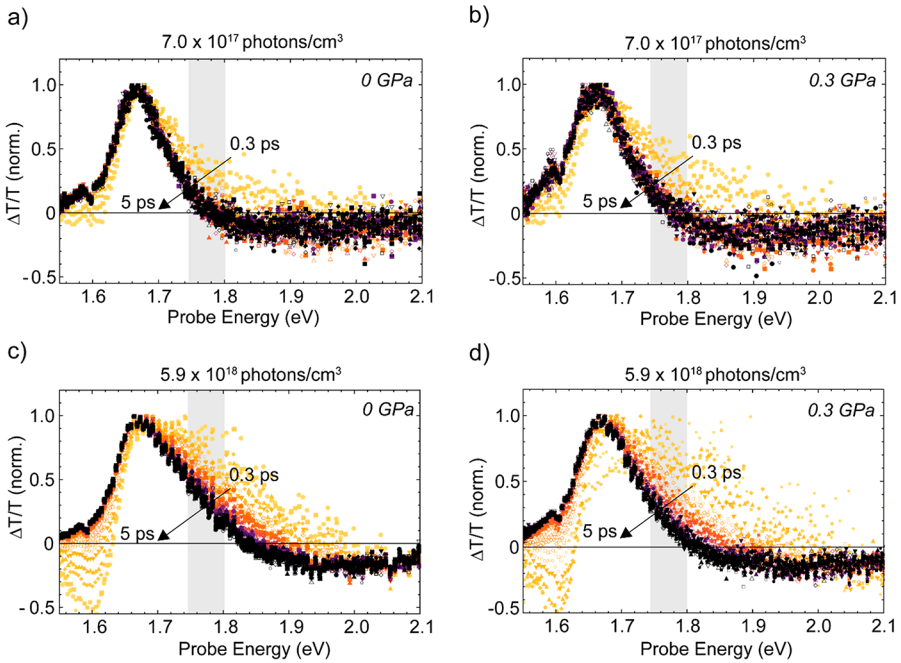

Figure 2. Charge-carrier cooling as a function of hydrostatic pressure measured by pressure-dependent transient absorption spectroscopy. $\Delta T/T$ traces of $MAPbI_3$ with an initial carrier concentration of 7.0×10^{17} photons/cm^3 (a) at ambient pressure and (b) at 0.3 GPa as a function of the probe energy. $\Delta T/T$ traces of $MAPbI_3$ with an initial carrier concentration of 5.9×10^{18} photons/cm^3 (c) at ambient pressure and (d) at 0.3 GPa as a function of probe energy.

inefficient if no thermal management strategy is applied. If the acoustic phonon lifetime increases, the HCC is expected to become faster. Understanding how lattice properties relate with HCC provides insights into the electronic behavior of devices operating at different charge-carrier densities. Thus, an effective strategy for manipulating *ad hoc* the HCC time is required to design devices with targetedapplications operating in a certain charge-carrier density regime.

In this work, we combine pressure-dependent femtosecond transient absorption spectroscopy (fs-TAS) and electron−phonon coupling calculations to elucidate the effect of lattice compression on the factors that influence the HCC. We use pressure-dependent fs-TAS to experimentally probe the HCC time in $MAPbI_3$ at room temperature at pressures ranging from 0 to 0.3 GPa at varying light intensities. At a low excitation density (7×10^{17} photons/cm^3), the HCC time is fast (0.3−0.5 ps) and independent of pressure. A high excitation density (>10^{18} photons/cm^3) triggers a Mott transition, previously calculated to occur at an excitation density of >7×10^{17} photons/cm^3.[21] We refer to the "Mott transition" as a change in electronic species from isolated polarons acting independently of an electron−hole plasma where the thermal energy is shared between overlapping polarons. At an excitation density above the Mott transition threshold (5.9×10^{18} photons/cm^3), the HCC is significantly slower (2−3 ps) at ambient pressure but accelerates by a factor of 2−3 with an increase in pressure to 0.3 GPa. In solar cells and optoelectronic devices operating above the Mott transition (>10^{18} photons/cm^3), a faster HCC time scale may allow for a faster dissipation of heat and therefore a lower operating temperature.

Solution-processed $MAPbI_3$ thin films were deposited by spin coating onto quartz substrates as reported in the Methods. Absorbance measurements as a function of pressure and X-ray diffraction measurements were performed on the sample to confirm the bandgap energy and the high crystallinity of the sample (Figure S1). Pressure-dependent transient absorption measurements were performed inside a hydrostatic pressure cell filled with the inert hydraulic liquid tetradecafluorohexane

https://doi.org/10.1021/acs.jpclett.1c00676
J. Phys. Chem. Lett. 2021, 12, 4118−4124

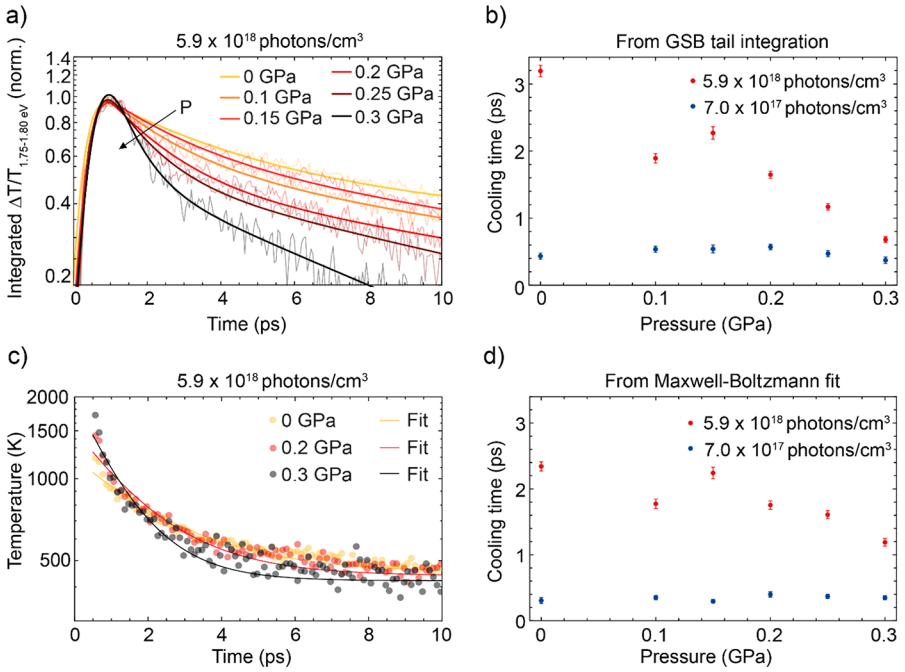

Figure 3. Two fitting strategies for determining the HCC time as a function of pressure. (a) Normalized $\Delta T/T$ integrated in the range of 1.75−1.80 eV in the GSB tail as a function of time and delay time for an excitation density of 5.9×10^{18} photons/cm^3 at different applied pressures. The decay of the GSB tail becomes faster with an increase in pressure. (b) HCC time extracted from the fit of the tail decay as a function of pressure above (red) and below the Mott transition threshold (blue). (c) Carrier temperature obtained by fitting the high-energy tail of the GSB with a Maxwell−Boltzmann distribution, as a function of delay time for a high excitation density of 5.9×10^{18} photons/cm^3 at different applied pressures. (d) HCC time obtained from the fit of the temperature decay as a function of pressure above (red) and below (blue) the Mott transition threshold.

[FC-72 (see Methods)] as depicted in Figure 1a. A 100 fs pulsed pump beam with an energy of 3.1 eV is used to photoexcite the sample, whereas a 100 fs pulsed probe beam (white light) is used to probe the excitation-induced change in transmission of $MAPbI_3$ on a picosecond time scale. The two beams are overlapped on the sample inside the pressure cell, and the arrival time of the two pulses is controlled with a delay stage. To ensure the absence of any nonlinear effects, we investigated the HCC process at excitation densities above the Mott transition, but where the $\Delta T/T$ still exhibits linear behavior with the pump fluence (Figure S2).

Photoexcitation with a photon energy larger than the $MAPbI_3$ bandgap led to a population of high-energy carriers (electrons and holes) with no common temperature (Figure 1b, dark red curve) that undergo rapid (~85 fs) thermalization, faster than our temporal resolution. This thermalization process results from carrier−carrier scattering. The resulting hot-carrier population can be described as a quasi-Fermi distribution. Once the hot-carrier population reaches a common temperature T_c (Figure 1b, red curve), higher than the lattice temperature T_L, carrier−phonon interactions dominate the HCC until T_c is in equilibrium with T_L (Figure 1b, yellow curve).

Panels a−d of Figure 2 show representative ultrafast transient absorption traces for a pump−probe delay between 0 and 5 ps of $MAPbI_3$ photoexcited at 3.1 eV (bandgap of 1.7 eV) with an initial carrier density n_0 of 7.0×10^{17} photons/cm^3 (Figure 2a,b) and 5.9×10^{18} photons/cm^3 (Figure 2c,d) at ambient pressure and at 0.3 GPa, respectively. The carrier density is calculated as described in Supplementary Note 1. No degradation is observed at a high excitation density as demonstrated in Figure S3 from the stability of the TA signal over the course of the measurement. The $\Delta T/T$ traces show three features: (i) a positive $\Delta T/T$ centered at the bandgap energy of ~1.67 eV corresponding to the ground state bleach (GSB) signal that results from the band filling effect, (ii) a negative $\Delta T/T$ feature at energies below the bandgap (<1.67 eV) at early times resulting from the bandgap decrease induced by the high energy carriers,[2] and (iii) a negative and broad $\Delta T/T$ signal at energies above the bandgap ($\gtrsim$1.7 eV) resulting from light absorption of the photogenerated carriers. Pseudocolor TA plots of the same sample as a function of the pump−probe delay and probe energy are reported in Figure S4.

The hot-carrier population is evident from the width of the initial GSB signal, which shrinks over the course of the measurement (picosecond time scale) as the hot carriers cool to the lattice temperature. This feature represents an average of the hot electron and hot hole temperatures given the effective masses are very similar.[28]

A comprehensive model to obtain the HCC time from the transient absorption measurements has still to be developed, but several methods are commonly used to obtain the HCC time and temperature.[13,16,29] We use two fitting strategies to obtain the trend of the HCC time as a function of pressure and excitation density. Both strategies yield a comparable HCC time with an increase in pressure and for both excitation densities. The first method consists of integrating the $\Delta T/T$ in the region of the high-energy GSB tail from 1.75 to 1.80 eV and plotting the result as a function of delay time. The integrated range is highlighted in gray in Figure 2. We plot the integrated traces for the high-density regime in Figure 3a. We fit the traces at fluences below and above the Mott transition with a convolution of the instrumental response function (IRF) and an exponential decay function (see Supplementary Note 2 for the analytical function and Figure S5 for the IRF

https://doi.org/10.1021/acs.jpclett.1c00676
J. Phys. Chem. Lett. 2021, 12, 4118−4124

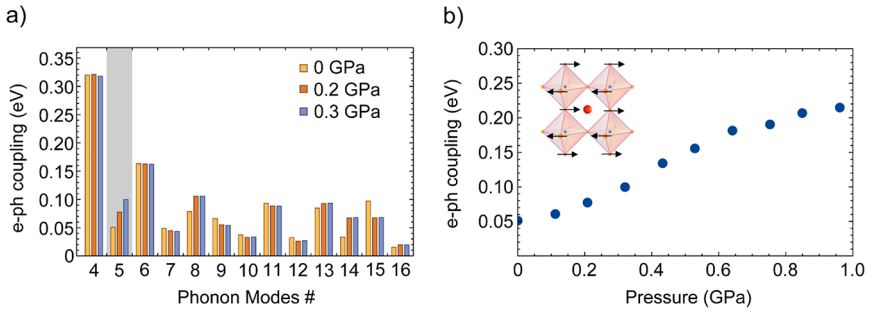

Figure 4. (a) Strength of electron−phonon coupling of the $MAPbI_3$ phonon modes to the conduction band minimum (CBM) at the Γ point in the Brillouin zone in a 2 × 2 × 2 supercell, listed in ascending phonon energy. Highlighted in gray is phonon mode 5 (~27 cm^{-1}, ~0.8 THz), affected most strongly by pressure. (b) Electron−phonon coupling of mode 5 (~27 cm^{-1}, ~0.8 THz) as a function of pressure. The inset shows atomic motions related to phonon mode 5 (octahedral twist).

fit). Below the Mott transition threshold (7×10^{17} photons/cm^3), no pressure dependency is observed, showing fast (~0.3 ps) HCC at all pressures investigated (Figure 3b, blue). Above the Mott transition threshold, the decay comprises a fast component with a time constant of a few picoseconds (attributed to the HCC) and a slow component with a time constant on the order of tens of picoseconds. The presence of an additional slower process above the Mott transition has been shown previously, and its origin is still under debate;[13,14,30,31] therefore, we compare the two fast components at the two excitation densities used. The time constant for the short-lived component above the Mott transition is plotted in Figure 3b (red). This experiment, contrary to the one below the Mott transition threshold, shows almost 3 times faster HCC (time constant of ~1 ps) at 0.3 GPa compared to that at ambient pressure (~3 ps).

To make sure the extracted trend of the HCC time with pressure is not affected by the energy range integrated, we performed the same fit but integrating $\Delta T/T$ in various energy ranges of the broad tail (Figures S6 and S7 above and below the Mott transition threshold, respectively). The absolute values of the HCC time constants slightly vary, but the trend as a function of pressure is consistent. The second method used to obtain the HCC time consists of approximating the high-energy tail of the GSB and the negative PIA[14] with a modified Maxwell−Boltzmann distribution function[13,32,33] as reported in Supplementary Note 3. The fit yields the carrier temperatures shown in Figure 3c as a function of delay time for ambient pressure and two representative high-pressure conditions. The initial temperature depends on the excess energy of the photoinduced carriers, and the excitation density. This is the temperature reached by the carriers directly after the thermalization. Interestingly, we observe a higher initial hot-carrier temperature with an increase in pressure. The slight red-shift in the bandgap energy [7 meV (Figure S8)] when we increase the pressure cannot account for this effect. We thus conclude that pressure may have an effect on the thermalization process, as well, but because this process is faster than our temporal resolution, we cannot further investigate this effect. The cooling time plotted in Figure 3d for the regime below and above the Mott transition (in blue and red, respectively) is obtained by fitting an exponential decay function to the curve in Figure 3c, taking into account the temperature errors of each data point. The HCC at ambient pressure is much slower than at high pressure, as reflected in a longer HCC time. The absolute values obtained by this fitting procedure for the cooling time are slightly lower than those obtained with the integration method shown in Figure 3b. As before, below the Mott transition threshold, HCC is fast, and there is no variation within the experimental error. In the regime above the Mott transition, we find again that the HCC is 2−3 times faster between 0 and 0.3 GPa, the same result obtained with the integration model.

It is well-established that the HCC time depends on experimental parameters like the ambient temperature, the excess of excitation energy compared to the bandgap of the material, and the excitation density.[3,20,34] We can exclude significant changes in these parameters (see Supplementary Note 4 for details) with a change in pressure, and therefore, we can attribute the pressure-dependent trend observed solely to changes in the material properties following compression, in particular in the electron−phonon coupling.

To understand what is happening on a microscopic scale within the material as a function of pressure, we calculate the electron−phonon coupling for all of the phonon modes. The results of the relevant phonon modes are shown in Figure 4a. In these calculations, we uniformly increase the pressure in a semilocal DFT electronic structure calculation (see Methods), starting with an ambient-pressure pseudocubic $MAPbI_3$ structure.[35] The number of phonon modes shown in Figure 4a is the index in ascending energy order. A detailed assignment and description of the phonon modes can be found in Supplementary Note 5 and is reported by Leguy et al.[36] Previous works[37,38] have shown that the dominant phonon mode coupled to the excited state dynamics observed by fs-TAS in $MAPbI_3$ has a frequency of ~27 cm^{-1} (~0.8 THz) and that there is a somewhat less strongly coupled mode at higher frequencies. For this reason, we confine our discussion to phonon modes 4−9, representing octahedral twist and distortion, as these are the most relevant for the coupling with the electrons at the conduction band minimum. Whereas most phonon modes show no clear trend with pressure, the electron−phonon coupling of mode 5 (~27 cm^{-1}, ~0.8 THz) associated with the octahedral twist, highlighted in gray in Figure 4a, shows a significant and approximately linear increase (Figure 4b) when the pressure increases from ambient pressure to 1 GPa, with a 2-fold enhancement at 0.3 GPa compared to ambient pressure.

A quantitative prediction of HCC (a phenomenological quantity) from the calculation of microscopic electron−phonon coupling matrix elements requires a mechanistic model of the cooling processes, and a detailed consideration of the electron−phonon interaction across the double electron

https://doi.org/10.1021/acs.jpclett.1c00676
J. Phys. Chem. Lett. 2021, 12, 4118−4124

and phonon Brillouin zones. This is beyond the scope of this work.

One would anticipate that the greater electron−phonon coupling at a higher pressure would result in faster HCC, both below and above the Mott transition. However, we observe a dependence on pressure only above the Mott transition threshold. Below that, HCC is fast (0.3−0.5 ps) and independent of pressure. In a polar material, the dielectric electron−phonon coupling dominates because it is long-range[39] and will provide the main channel by which electrons photoexcited above the bandgap will lose their energy. This coupling involves the interaction of the charge of the carriers with the transition dipole moment of the surrounding phonon modes. The variational polaron method predicts a polaron relaxation time constant of ∼0.1 ps[40] for this material, which is consistent with our observation of a very short HCC time. This long-range dielectric coupling is not expected to be significantly affected by pressure,[41] in agreement with our observations.

Above the threshold for the Mott transition, we propose that this dielectric coupling is screened, and instead, the HCC proceeds via the weaker local electron−phonon coupling. We calculate that this local electron−phonon coupling is proportional to pressure over the pressure range of 0−0.3 GPa (in fact we find a linear trend up to 1.0 GPa), so the HCC above the Mott transition becomes faster with pressure. This result is related to what has been found by Mohanan et al.,[42] who attributed the presence of a hot-phonon bottleneck to the deposition of a large portion of the initial energy on the optical modes at 27 cm^{-1} (∼0.8 THz). These do not efficiently dissipate the excess energy as they are isolated from the rest of the lattice.Our findings thus reveal that enhancement of the of the electron−phonon coupling under pressure can be used to manipulate HCC at densities above the Mott transition density, while having no effect in the regime below, where long-range dielectric electron−phonon coupling dominates. The excitation density that we assign for the Mott transition comes from considering the polaron size. An alternative interpretation of the observed pressure dependence of the cooling time could be that this Mott transition is being pushed to a higher density under pressure. This change would require that the polarons be more localized at higher pressures. In turn, within the Fröhlich theory, this would require a considerably larger dielectric electron−phonon coupling, or a considerably larger effective mass. However, we are cautious with this interpretation as the vibrational and optical properties do not change significantly over this pressure range.

The hot-phonon bottleneck in a $MAPbI_3$ perovskite has also been attributed to the extremely short acoustic phonon lifetime[43] of this material, which also causes its low thermal conductivity.[44] A short acoustic phonon lifetime can thus be responsible for the suppression of heat dissipation, as this energy could be reabsorbed by optical phonons and thus create a hot-phonon bottleneck that slows the cooling of the hot electron−phonon plasma. Although this mechanism occurs in the second stage of the cooling (tens of picoseconds), it might have some minor influence on the first cooling stage, as well. Determining the extent to which the faster HCC results from only the enhanced electron−phonon coupling or from a combination with a longer acoustic phonon lifetime would require an expensive computation that is beyond the scope of this work.

In conclusion, we used pressure-dependent fs-TAS to investigate the effect of external pressure on hot-carrier cooling in $MAPbI_3$ thin films. We found that below the Mott transition threshold, the HCC time is not affected by pressure, whereas it becomes 2−3 times faster above the Mott transition. Our calculations reveal a 2-fold enhancement of the electron−phonon coupling for the mode related to the octahedral twist when the pressure is increased from ambient pressure to 0.3 GPa. These findings, together with the observed difference in the behavior in the low- and high-density regime, suggest the presence of two different mechanisms dominating HCC at the two excitation densities explored. Below the Mott transition threshold, where polarons do not overlap, the long-range dielectric electron−phonon coupling dominates. Above the Mott transition threshold, this contribution is suppressed as the polarization fields of the polarons overlap forming an electron−hole plasma and the HCC occurs via local electron−phonon coupling. This local contribution is significantly weaker at ambient pressure, leading to slow HCC, but increases linearly over the 0.3 GPa pressure range studied. These findings contribute to the understanding of how applied stress can be used to control the HCC time in halide perovskite devices for emissive applications such as lasers and single-photon sources.

■ ASSOCIATED CONTENT

Supporting Information

The Supporting Information is available free of charge at https://pubs.acs.org/doi/10.1021/acs.jpclett.1c00676.

Methods, Absorption and XRD spectra of $MAPbI_3$ thin films, $\Delta T/T$ as a function of probe energy and real time for $MAPbI_3$ at ambient pressure for degradation, two-dimensional plot of $\Delta T/T$ as a function of probe energy and time for $MAPbI_3$ at ambient pressure and 0.3 GPa, IRF as a function of pressure calculated from $MAPbI_3$ excited resonantly at 800 nm, cooling time extracted from the integration of $\Delta T/T$ in various energy ranges of the broad tail as a function of pressure in the low- and high-density regime, $MAPbI_3$ bandgap as a function of pressure, excitation density calculation, fitting function for $\Delta T/T$ decay in the high-energy tail, influence of experimental conditions on HCC time, and assignment of the optical modes (PDF)

■ AUTHOR INFORMATION

Corresponding Author

Bruno Ehrler − *Center for Nanophotonics, AMOLF, 1098 XG Amsterdam, The Netherlands;* orcid.org/0000-0002-5307-3241; Email: b.ehrler@amolf.nl

Authors

Loreta A. Muscarella − *Center for Nanophotonics, AMOLF, 1098 XG Amsterdam, The Netherlands;* orcid.org/0000-0002-0559-4085

Eline M. Hutter − *Center for Nanophotonics, AMOLF, 1098 XG Amsterdam, The Netherlands; Department of Chemistry, Utrecht University, 3584 CB Utrecht, The Netherlands;* orcid.org/0000-0002-5537-6545

Jarvist M. Frost − *Department of Physics, Imperial College London, London SW7 2AZ, United Kingdom;* orcid.org/0000-0003-1938-4430

Gianluca G. Grimaldi − *Center for Nanophotonics, AMOLF, 1098 XG Amsterdam, The Netherlands; Cavendish Laboratory, Cambridge, Cambridge CB3 0HE, United Kingdom;* orcid.org/0000-0002-2626-9118
Jan Versluis − *Center for Nanophotonics, AMOLF, 1098 XG Amsterdam, The Netherlands*
Huib J. Bakker − *Center for Nanophotonics, AMOLF, 1098 XG Amsterdam, The Netherlands;* orcid.org/0000-0003-1564-5314

Complete contact information is available at: https://pubs.acs.org/10.1021/acs.jpclett.1c00676

Notes

The authors declare no competing financial interest.

■ ACKNOWLEDGMENTS

The work of L.A.M., E.M.H., J.V., H.J.B., and B.E. is part of the Dutch Research Council (NWO) and was performed at the research institute AMOLF. The work of L.A.M. was supported by NWO Vidi Grant 016.Vidi.179.005. The authors thank Henk-Jan Boluijt for the design of Figure 1a. The authors thank María C. Gélvez-Rueda for commenting on the manuscript. J.M.F. is supported by a Royal Society University Research Fellowship (URF-R1-191292). Electronic structure calculations used the Imperial College Research Computing Service (DOI: 10.14469/hpc/2232). The work of G.G.G. was supported by the EPSRC International Centre to Centre Grant EP/S030638/1.

■ REFERENCES

(1) Richter, J. M.; Branchi, F.; Valduga de Almeida Camargo, F.; Zhao, B.; Friend, R. H.; Cerullo, G.; Deschler, F. Ultrafast Carrier Thermalization in Lead Iodide Perovskite Probed with Two-Dimensional Electronic Spectroscopy. *Nat. Commun.* **2017**, *8* (1), 376.
(2) Shah, J. *Ultrafast Spectroscopy of Semiconductors and Semiconductor Nanostructures*; 1999.
(3) Fu, J.; Xu, Q.; Han, G.; Wu, B.; Huan, C. H. A.; Leek, M. L.; Sum, T. C. Hot Carrier Cooling Mechanisms in Halide Perovskites. *Nat. Commun.* **2017**, *8* (1), 1300.
(4) Ziaja, B.; Medvedev, N.; Tkachenko, V.; Maltezopoulos, T.; Wurth, W. Time-Resolved Observation of Band-Gap Shrinking and Electron-Lattice Thermalization within X-Ray Excited Gallium Arsenide. *Sci. Rep.* **2016**, DOI: 10.1038/srep18068.
(5) Polman, A.; Atwater, H. A. Photonic Design Principles for Ultrahigh-Efficiency Photovoltaics. *Nat. Mater.* **2012**, *11*, 174.
(6) Alharbi, F. H.; Kais, S. Theoretical Limits of Photovoltaics Efficiency and Possible Improvements by Intuitive Approaches Learned from Photosynthesis and Quantum Coherence. *Renewable Sustainable Energy Rev.* **2015**, *43*, 1073.
(7) Haque, M. A.; Kee, S.; Villalva, D. R.; Ong, W. L.; Baran, D. Halide Perovskites: Thermal Transport and Prospects for Thermoelectricity. *Adv. Sci.* **2020**, *7*, 1903389.
(8) Kahmann, S.; Loi, M. A. Hot Carrier Solar Cells and the Potential of Perovskites for Breaking the Shockley-Queisser Limit. *J. Mater. Chem. C* **2019**, *7*, 2471.
(9) Fehse, R.; Tomić, S.; Adams, A. R.; Sweeney, S. J.; O'Reilly, E. P.; Andreev, A.; Riechert, H. A Quantitative Study of Radiative, Auger, and Defect Related Recombination Processes in 1.3-Mm GaInNAs-Based Quantum-Well Lasers. *IEEE J. Sel. Top. Quantum Electron.* **2002**, *8*, 801.
(10) Kim, J. H.; Ko, Y. H.; Gong, S. H.; Ko, S. M.; Cho, Y. H. Ultrafast Single Photon Emitting Quantum Photonic Structures Based on a Nano-Obelisk. *Sci. Rep.* **2013**, DOI: 10.1038/srep02150.
(11) Wang, C. Y.; Liu, M.; Feng, M.; Holonyak, N. Microwave Extraction Method of Radiative Recombination and Photon Lifetimes up to 85 °C on 50 Gb/s Oxide-Vertical Cavity Surface Emitting Laser. *J. Appl. Phys.* **2016**, *120*, 223103.
(12) Yang, Y.; Ostrowski, D. P.; France, R. M.; Zhu, K.; Van De Lagemaat, J.; Luther, J. M.; Beard, M. C. Observation of a Hot-Phonon Bottleneck in Lead-Iodide Perovskites. *Nat. Photonics* **2016**, *10*, 53.
(13) Verma, S. D.; Gu, Q.; Sadhanala, A.; Venugopalan, V.; Rao, A. Slow Carrier Cooling in Hybrid Pb-Sn Halide Perovskites. *ACS Energy Lett.* **2019**, *4* (3), 736−740.
(14) Yang, J.; Wen, X.; Xia, H.; Sheng, R.; Ma, Q.; Kim, J.; Tapping, P.; Harada, T.; Kee, T. W.; Huang, F.; et al. Acoustic-Optical Phonon up-Conversion and Hot-Phonon Bottleneck in Lead-Halide Perovskites. *Nat. Commun.* **2017**, *8*, 1−9.
(15) Wen, Y. C.; Chen, C. Y.; Shen, C. H.; Gwo, S.; Sun, C. K. Ultrafast Carrier Thermalization in InN. *Appl. Phys. Lett.* **2006**, *89*, 232114.
(16) Price, M. B.; Butkus, J.; Jellicoe, T. C.; Sadhanala, A.; Briane, A.; Halpert, J. E.; Broch, K.; Hodgkiss, J. M.; Friend, R. H.; Deschler, F. Hot-Carrier Cooling and Photoinduced Refractive Index Changes in Organic-Inorganic Lead Halide Perovskites. *Nat. Commun.* **2015**, *6*, 8420.
(17) Chen, J.; Messing, M. E.; Zheng, K.; Pullerits, T. Cation-Dependent Hot Carrier Cooling in Halide Perovskite Nanocrystals. *J. Am. Chem. Soc.* **2019**, *141* (8), 3532−3540.
(18) Shi, H.; Zhang, X.; Sun, X.; Zhang, X. Strong Hot-Phonon Bottleneck Effect in All-Inorganic Perovskite Nanocrystals. *Appl. Phys. Lett.* **2020**, *116*, 151902.
(19) Hopper, T. R.; Gorodetsky, A.; Frost, J. M.; Müller, C.; Lovrincic, R.; Bakulin, A. A. Ultrafast Intraband Spectroscopy of Hot-Carrier Cooling in Lead-Halide Perovskites. *ACS Energy Lett.* **2018**, *3* (9), 2199−2205.
(20) Bretschneider, S. A.; Ivanov, I.; Wang, H. I.; Miyata, K.; Zhu, X.; Bonn, M. Quantifying Polaron Formation and Charge Carrier Cooling in Lead-Iodide Perovskites. *Adv. Mater.* **2018**, *30* (29), 1707312.
(21) Frost, J. M.; Whalley, L. D.; Walsh, A. Slow Cooling of Hot Polarons in Halide Perovskite Solar Cells. *ACS Energy Lett.* **2017**, *2* (12), 2647−2652.
(22) Sendner, M.; Nayak, P. K.; Egger, D. A.; Beck, S.; Müller, C.; Epding, B.; Kowalsky, W.; Kronik, L.; Snaith, H. J.; Pucci, A.; et al. Optical Phonons in Methylammonium Lead Halide Perovskites and Implications for Charge Transport. *Mater. Horiz.* **2016**, *3* (6), 613−620.
(23) Price, M. B.; Butkus, J.; Jellicoe, T. C.; Sadhanala, A.; Briane, A.; Halpert, J. E.; Broch, K.; Hodgkiss, J. M.; Friend, R. H.; Deschler, F. Hot-Carrier Cooling and Photoinduced Refractive Index Changes in Organic-Inorganic Lead Halide Perovskites. *Nat. Commun.* **2015**, *6*, 8420 DOI: 10.1038/ncomms9420.
(24) Li, M.; Bhaumik, S.; Goh, T. W.; Kumar, M. S.; Yantara, N.; Grätzel, M.; Mhaisalkar, S.; Mathews, N.; Sum, T. C. Slow Cooling and Highly Efficient Extraction of Hot Carriers in Colloidal Perovskite Nanocrystals. *Nat. Commun.* **2017**, *8* (1), 14350.
(25) Li, B.; Kawakita, Y.; Liu, Y.; Wang, M.; Matsuura, M.; Shibata, K.; Ohira-Kawamura, S.; Yamada, T.; Lin, S.; Nakajima, K.; et al. Polar Rotor Scattering as Atomic-Level Origin of Low Mobility and Thermal Conductivity of Perovskite CH 3 NH 3 PbI 3. *Nat. Commun.* **2017**, DOI: 10.1038/ncomms16086.
(26) Beecher, A. N.; Semonin, O. E.; Skelton, J. M.; Frost, J. M.; Terban, M. W.; Zhai, H.; Alatas, A.; Owen, J. S.; Walsh, A.; Billinge, S. J. L. Direct Observation of Dynamic Symmetry Breaking above Room Temperature in Methylammonium Lead Iodide Perovskite. *ACS Energy Lett.* **2016**, *1*, 880.
(27) Nolas, G. S.; Goldsmid, H. J. Thermal Conductivity of Semiconductors. In *Thermal Conductivity*; 2006.
(28) Giorgi, G.; Fujisawa, J. I.; Segawa, H.; Yamashita, K. Small Photocarrier Effective Masses Featuring Ambipolar Transport in

Methylammonium Lead Iodide Perovskite: A Density Functional Analysis. *J. Phys. Chem. Lett.* **2013**, *4*, 4213.
(29) Lim, J. W. M.; Giovanni, D.; Righetto, M.; Feng, M.; Mhaisalkar, S. G.; Mathews, N.; Sum, T. C. Hot Carriers in Halide Perovskites: How Hot Truly? *J. Phys. Chem. Lett.* **2020**, *11*, 2743.
(30) Senellart, P.; Solomon, G.; White, A. High-Performance Semiconductor Quantum-Dot Single-Photon Sources. *Nat. Nanotechnol.* **2017**, *12*, 1026.
(31) Savill, K. J.; Klug, M. T.; Milot, R. L.; Snaith, H. J.; Herz, L. M. Charge-Carrier Cooling and Polarization Memory Loss in Formamidinium Tin Triiodide. *J. Phys. Chem. Lett.* **2019**, *10*, 6038.
(32) Von Der Linde, D.; Lambrich, R. Direct Measurement of Hot-Electron Relaxation by Picosecond Spectroscopy. *Phys. Rev. Lett.* **1979**, *42*, 1090.
(33) Zanato, D.; Balkan, N.; Ridley, B. K.; Hill, G.; Schaff, W. J. Hot Electron Cooling Rates via the Emission of LO-Phonons in InN. *Semicond. Sci. Technol.* **2004**, *19*, 1024.
(34) Kawai, H.; Giorgi, G.; Marini, A.; Yamashita, K. The Mechanism of Slow Hot-Hole Cooling in Lead-Iodide Perovskite: First-Principles Calculation on Carrier Lifetime from Electron−Phonon Interaction. *Nano Lett.* **2015**, *15* (5), 3103−3108.
(35) Walsh, A.; elds22; Brivio, F.; Frost, J. M. *WMD-Group/Hybrid-Perovskites: Collection 1*; 2019.
(36) Leguy, A. M. A.; Goñi, A. R.; Frost, J. M.; Skelton, J.; Brivio, F.; Rodríguez-Martínez, X.; Weber, O. J.; Pallipurath, A.; Alonso, M. I.; Campoy-Quiles, M.; et al. Dynamic Disorder, Phonon Lifetimes, and the Assignment of Modes to the Vibrational Spectra of Methylammonium Lead Halide Perovskites. *Phys. Chem. Chem. Phys.* **2016**, *18* (39), 27051−27066.
(37) Guo, P.; Xia, Y.; Gong, J.; Cao, D. H.; Li, X.; Li, X.; Zhang, Q.; Stoumpos, C. C.; Kirschner, M. S.; Wen, H.; et al. Direct Observation of Bandgap Oscillations Induced by Optical Phonons in Hybrid Lead Iodide Perovskites. *Adv. Funct. Mater.* **2020**, *30* (22), 1907982.
(38) Park, M.; Neukirch, A. J.; Reyes-Lillo, S. E.; Lai, M.; Ellis, S. R.; Dietze, D.; Neaton, J. B.; Yang, P.; Tretiak, S.; Mathies, R. A. Excited-State Vibrational Dynamics toward the Polaron in Methylammonium Lead Iodide Perovskite. *Nat. Commun.* **2018**, *9* (1), 2525 DOI: 10.1038/s41467-018-04946-7.
(39) Giustino, F. Electron-Phonon Interactions from First Principles. *Rev. Mod. Phys.* **2017**, *89* (1), 015003 DOI: 10.1103/RevModPhys.89.015003.
(40) Frost, J. M. Calculating Polaron Mobility in Halide Perovskites. *Phys. Rev. B: Condens. Matter Mater. Phys.* **2017**, *96* (19), 195202 DOI: 10.1103/PhysRevB.96.195202.
(41) Francisco-López, A.; Charles, B.; Weber, O. J.; Alonso, M. I.; Garriga, M.; Campoy-Quiles, M.; Weller, M. T.; Goñi, A. R. Pressure-Induced Locking of Methylammonium Cations versus Amorphization in Hybrid Lead Iodide Perovskites. *J. Phys. Chem. C* **2018**, *122* (38), 22073−22082.
(42) Monahan, D. M.; Guo, L.; Lin, J.; Dou, L.; Yang, P.; Fleming, G. R. Room-Temperature Coherent Optical Phonon in 2D Electronic Spectra of CH3NH3PbI3 Perovskite as a Possible Cooling Bottleneck. *J. Phys. Chem. Lett.* **2017**, *8*, 3211.
(43) Gold-Parker, A.; Gehring, P. M.; Skelton, J. M.; Smith, I. C.; Parshall, D.; Frost, J. M.; Karunadasa, H. I.; Walsh, A.; Toney, M. F. Acoustic Phonon Lifetimes Limit Thermal Transport in Methylammonium Lead Iodide. *Proc. Natl. Acad. Sci. U. S. A.* **2018**, *115*, 11905.
(44) Pisoni, A.; Jaćimović, J.; Barišić, O. S.; Spina, M.; Gaál, R.; Forró, L.; Horváth, E. Ultra-Low Thermal Conductivity in Organic−Inorganic Hybrid Perovskite CH3NH3PbI3. *J. Phys. Chem. Lett.* **2014**, *5* (14), 2488−2492.

https://doi.org/10.1021/acs.jpclett.1c00676
J. Phys. Chem. Lett. 2021, 12, 4118−4124